ACS Catalysis

pubs.acs.org/acscatalysis

Research Article

Understanding the Atomic and Defective Interface Effect on Ruthenium Clusters for the Hydrogen Evolution Reaction

Taotao Gao, Xiangmin Tang, Xiaoqin Li, Shuaiwei Wu, Shumin Yu, Panpan Li,* Dan Xiao,* and Zhaoyu Jin*

Cite This: *ACS Catal.* 2023, 13, 49−59

Read Online

ACCESS | Metrics & More | Article Recommendations | Supporting Information

ABSTRACT: Water electrolysis powered by renewable electric energy is a promising technology for green hydrogen production without carbon emissions, while highly efficient and cost-effective electrocatalysts with long durability are urgently needed. Here, we demonstrate oxygen-coordinated single-atom iron sites ($Fe-O_4$) decorated carbon nanotubes with abundant vacancies as the substrate for stabilizing Ru clusters (CNT−V−Fe−Ru). The catalyst shows high performance for the hydrogen evolution reaction (HER) in both acidic and alkaline media, respectively. The HER kinetics analysis demonstrates that the defective substrate with single-atomic sites could significantly improve the intrinsic activity of Ru species. Theoretical calculations also support the superior HER behavior of CNT−V−Fe−Ru with fundamental insights into metal−substrate interactions. The present study highlights a unique feature of single-atom catalysts for serving as advanced supporting materials, which offers tremendous opportunities to adequately regulate electronic structures of metal−substrate interfaces at the atomic level.

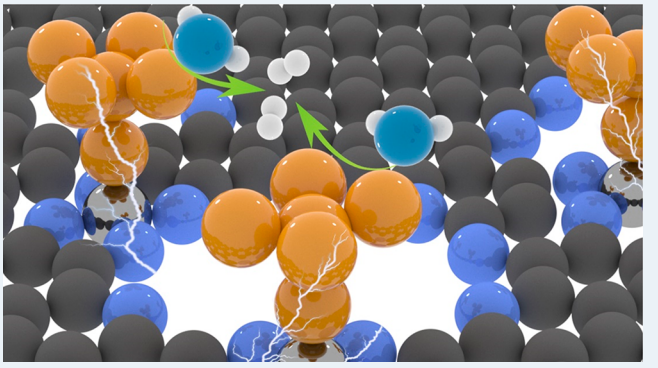

KEYWORDS: *electrocatalysis, single-atomic site, substrate effect, vacancy defect, hydrogen evolution reaction*

1. INTRODUCTION

Electrochemically producing molecular hydrogen from water has emerged as a key component of prospective clean-energy technologies.[1,2] The efficient and low-cost catalysts for the hydrogen evolution reaction (HER) are critical for the rapid development of hydrogen energy produced from water electrolysis powered by renewable electric energy.[2] Pt-based catalysts have so far shown state-of-the-art HER performance, while the scarce reserves and expensive prices substantially limit their large-scale commercial applications.[3,4] The relatively cost-effective ruthenium (Ru)-based materials have been extensively studied as potential substitutes as a result of similar physical as well as chemical properties with Pt and highly regulable electronic structures.[5−9] However, Ru-based catalysts still face significant challenges in improving their intrinsic activity for the HER. In particular, the high cohesive energy of Ru would lead to irreversible agglomeration and structural collapse during catalysis.[10,11] In addition, overstrong H adsorption intensity on Ru sites also prohibits the desorption step, thus resulting in the decreased HER performance.[12,13] Nevertheless, a few studies have demonstrated that the electronic structures of metal active sites could be effectively regulated through the interfacial interaction with substrates.[7,14−19] Therefore, the manipulation of binding moieties of metal−substrate interfaces would fundamentally address the hurdles that have confronted Ru and other transition metal-based catalysts.

The carbon-based substrates with outstanding electrical conductivity, large specific surface area, and highly regulable structure have been extensively studied for electrocatalysis.[20] Especially, the introduction of porous structure and heteroatoms (N, P, O, etc.) into carbon-based substrates efficiently increases the number of vacancy defects for stable immobilization of active sites with high dispersion.[7,10,21−24] However, there are considerable challenges in adequately adjusting electronic structures of metal−substrate interfaces at the atomic level via accessible regulation strategies. Notably, carbon-supported single-atomic catalysts have been paid great attention since the advent of remarkably improved atomic utilization with highly tailorable electronic structures in comparison to bulk and nanocatalysts.[25−32] In this regard, one would expect carbon-supported single-atom materials to serve as substrates for loading active metallic catalysts. Recent

Received: September 18, 2022
Revised: November 21, 2022
Published: December 12, 2022

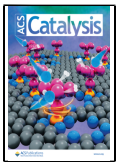

Downloaded via SHREENIVAS DESHPANDE LIBRARY IIT (BHU) VARANASI on July 23, 2026 at 07:07:32 (UTC).
See https://pubs.acs.org/sharingguidelines for options on how to legitimately share published articles.

ACS Publications

© 2022 American Chemical Society

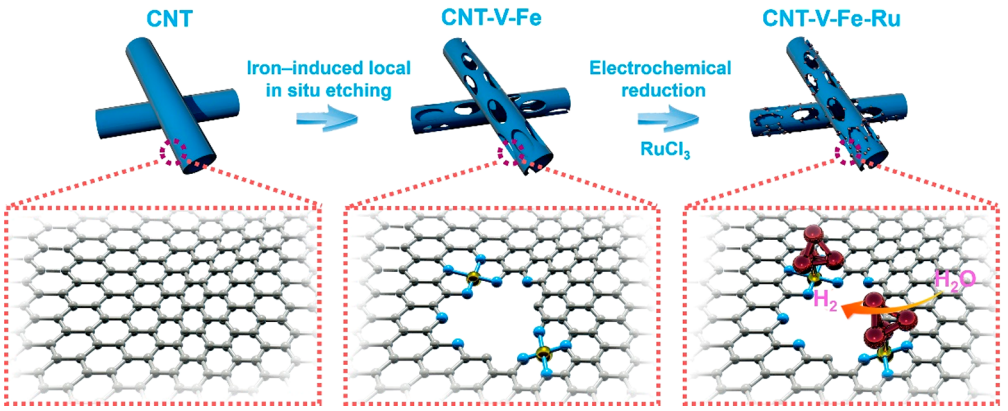

Figure 1. Schematic of the preparation process of CNT−V−Fe as well as CNT−V−Fe−Ru and the HER catalytic process on Ru sites.

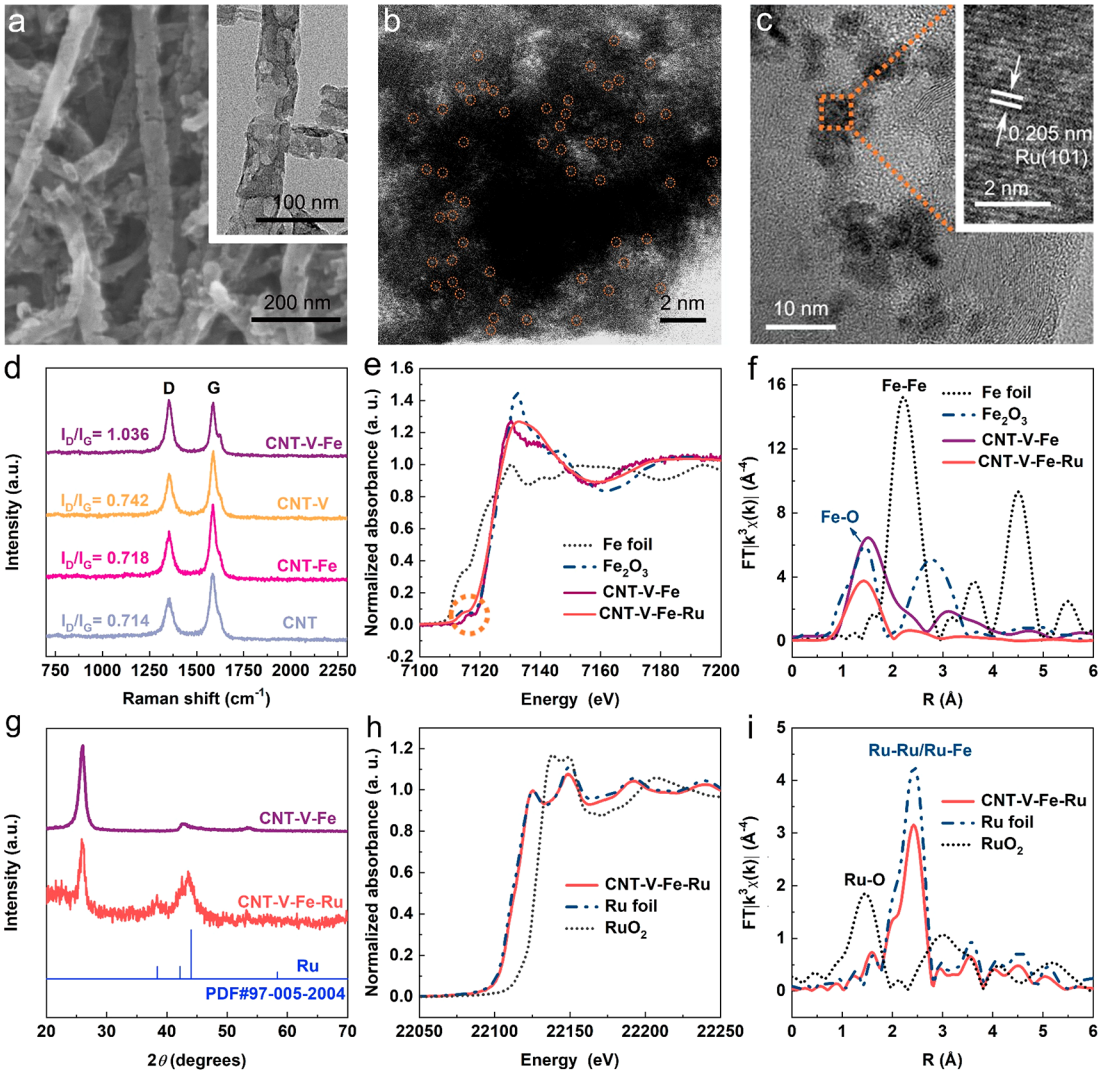

Figure 2. Morphological and structural characterizations. (a) SEM and TEM images (the inset) and (b) HAADF-STEM image of CNT−V−Fe. (c) HRTEM images of CNT−V−Fe−Ru; the lattice fringe of the Ru cluster (the inset). (d) Raman spectra of CNT, CNT−Fe, CNT−V, and CNT−V−Fe. (e) XANES and (f) FT-EXAFS of Fe foil, Fe_2O_3, CNT−V−Fe, and CNT−V−Fe−Ru; the intensity of Fe foil is halved. (g) XRD patterns of CNT−V−Fe−Ru and CNT−V−Fe. (h) XANES and (i) FT-EXAFS of Ru foil, RuO_2, and CNT−V−Fe−Ru.

literature has reported the synergistic enhancement of electrocatalytic performance enabled by single-atom decorated supports and platinum-group metal nanoparticles.[25,33,34] However, an in-depth mechanistic understanding of the interfacial interaction between single-atomic sites over substrates and metal active species is still elusive, while little knowledge about the effect of defects on the intrinsic activity has been demonstrated in the previous studies.

https://doi.org/10.1021/acscatal.2c04586
ACS Catal. 2023, 13, 49−59

Here, an iron-induced functionalization strategy is presented to prepare oxygen-coordinated single-atomic iron sites (Fe−O_4) with decorated vacancy-rich CNTs (CNT−V−Fe) as advanced substrates for supporting Ru clusters (CNT−V−Fe−Ru) with intrinsically improved HER activity in both acidic and alkaline media. The reported CNT−V−Fe can serve as a unique platform to strongly anchor Ru clusters, thus resulting in impressive durability for long-term electrolysis. Additionally, the synergistic combination of vacancy defects and iron single-atom sites promotes the charge redistribution of Ru clusters and adequately optimizes H adsorption energy. This study highlights the unique features of the defective single-atom supporting materials that can be rationally regulated in their electronic structures, particularly at metal−substrate interfaces, which are mutually beneficial to both activity and stability of electrocatalysts.

2. RESULTS AND DISCUSSION

2.1. Preparation and Characterization. Figure 1 displays the preparation process of CNT−V−Fe substrate with abundant vacancy defects and iron single-atom sites. Although CNTs have high thermal stability in the air, the metallic compounds can induce the oxidation of local carbon species at a temperature lower than the degradation temperature of CNTs. After loading pore-forming reagents (iron compounds) on CNTs, there is no obvious particle on the surface of CNT−Fe−OH according to the SEM image in Figure S1, and no XRD characteristic diffraction peak (Figure S2) assigned to iron-based compounds is observed. Therefore, the iron-based compounds with a small particle size are fully dispersed on the surface of CNTs, leading to the formation of abundant porous structures on CNTs during the heat treatment process. According to the TG and DTG curves of CNT and CNT−Fe−OH in Figure S3, the rapid carbon weight-loss temperature of the carbon species in CNT−Fe−OH (565 °C) is significantly lower than that of CNTs (603 °C), indicating that the introduction of iron compounds reduces the thermal stability of CNTs. The carbon species near iron compounds begin to degrade at 470 °C, while the degradation temperature of CNTs reaches 510 °C. The decrease in the thermal stability of the local carbon species makes the formation of porous structures in CNTs possible. The relatively unstable carbon species will react with the oxygen and then form porous structures with vacancy defects; meanwhile, the main backbone of CNTs is retained (Figure S4). Based on the temperature optimization (Figures 2a and S5), the heating temperature of 490 °C is used to prepare CNT−V−Fe with abundant defective porous structures; CNT−V−Fe is different from the CNTs with a smooth surface (Figure S6) and obtains a relatively complete main skeleton of CNTs. Although CNT−V, as a controlling sample, undergoes a similar treatment process to CNT−V−Fe except for introducing Fe compounds, it only shows a small number of porous structures (Figures S7, S8). These results further confirm that iron compounds are efficient pore-foaming agents to promote the formation of defective porous structures. To obtain the comparison of the CNT−Fe substrate with the iron sites and without defect, the CNT−Fe−OH is heated under the argon flow and other preparation conditions are the same as those of CNT−V−Fe. CNT−Fe shows a smooth surface (Figure S9). The iron is uniformly distributed on the surface of CNT−Fe according to the element mapping of Fe (Figure S10), and the iron content is 0.03 wt % based on the ICP-AES experiment (Table S1).

The creation of a defective porous structure is beneficial to enlarging the specific surface area and increasing the number of vacancy defects, which has a positive effect on enhancing the reaction rate and activity. According to the nitrogen adsorption−desorption curves (Figure S11a), CNT−V−Fe obtains the highest (Brunauer−Emmett−Teller) BET-specific surface area (195.2 $m^2\ g^{-1}$, Table S2), which is significantly higher than those of CNT (81.7 $m^2\ g^{-1}$), CNT−Fe (82.1 $m^2\ g^{-1}$), and CNT−V (116.9 $m^2\ g^{-1}$) because of the formation of more porous structures. In addition, CNT−V−Fe possesses larger pore size distributions than CNT, CNT−Fe, and CNT−V (Figure S11b), suggesting better mass transfer in electrocatalysis. As shown in the HRTEM image of CNT−V−Fe and the corresponding fast Fourier transform (FFT) patterns (Figure S12 and the inset), the fracture and increased level of confusion for lattice fringes near the porous structures can be observed, indicating that the formation process of porous structures is accompanied by the increase of vacancy defects and the decrease in the degree of graphitization of carbon. In addition, the ratio of the peak intensities of the D peak (1342 cm^{-1}) and G peak (1570 cm^{-1}) for the samples from low to high in order is CNT (I_D/I_G = 0.714), CNT−Fe (I_D/I_G = 0.718), CNT−V (I_D/I_G = 0.742), and CNT−V−Fe (I_D/I_G = 1.036) based on the Raman spectra in Figure 2d. The higher I_D/I_G ratio denotes the CNT−V−Fe with more vacancy defects and a lower degree of graphitization of carbon due to the formation of defect-rich porous structures,[35−37] which is consistent with the result of HRTEM images (Figure S12). More importantly, the main structure of CNT is successfully retained during the preparation processes according to the SEM and TEM images (Figure 2a) and the XRD pattern of CNT−V−Fe (Figure S13).

The HAADF-STEM image with aberration correction and XPS spectra are used to further analyze the composition and structure of CNT−V−Fe. The HAADF-STEM images (Figures 2b and S14) also display a porous structure in CNT−V−Fe, and the isolated bright spots (ca. 0.1 nm in diameter) are observed, indicating that the isolated iron single atoms are decorated on CNT−V−Fe during the etching process. Moreover, the XPS spectra further confirm the presence of C, O, and Fe in CNT−V−Fe (Figure S15), and the introduction of iron increases the oxygen content (Figure S16 and Table S3). The binding energy at ca. 531.8 eV (O 1s XPS spectrum in Figure S15c) also indicates the formation of C−O−Fe species.[38,39] Nevertheless, the oxidation state and fine structure of the iron single atom are not well substantiated only based on the single XPS analysis because of the low content of Fe species in CNT−V−Fe (0.15 wt % based on the inductively coupled plasma analysis, Table S1).

XAFS spectroscopy is a powerful technique to precisely analyze the fine structure, such as the coordination environment and chemical state, of metal centers. Figure 2e displays the Fe K-edge XANES of CNT−V−Fe, Fe_2O_3, and Fe foil. The rising-edge position at ca. 7120.6 eV and the obvious pre-edge peak at ca. 7115.6 eV for CNT−V−Fe are close to Fe_2O_3, suggesting that the oxidation state of iron is about +3. In addition, the first derivative of the XANES signal of CNT−V−Fe is different from that of Fe_2O_3 (Figure S17), which is ascribed to the unique planar geometry of the oxygen-coordinated single-atomic iron sites (Fe−O_4).[38] The Fourier transform of Fe K-edge EXAFS (FT-EXAFS) in Figure 2f suggests that the iron atom is mainly coordinated with O atoms (the peak at ca. 1.52 Å) rather than other Fe atoms

https://doi.org/10.1021/acscatal.2c04586
ACS Catal. 2023, 13, 49−59

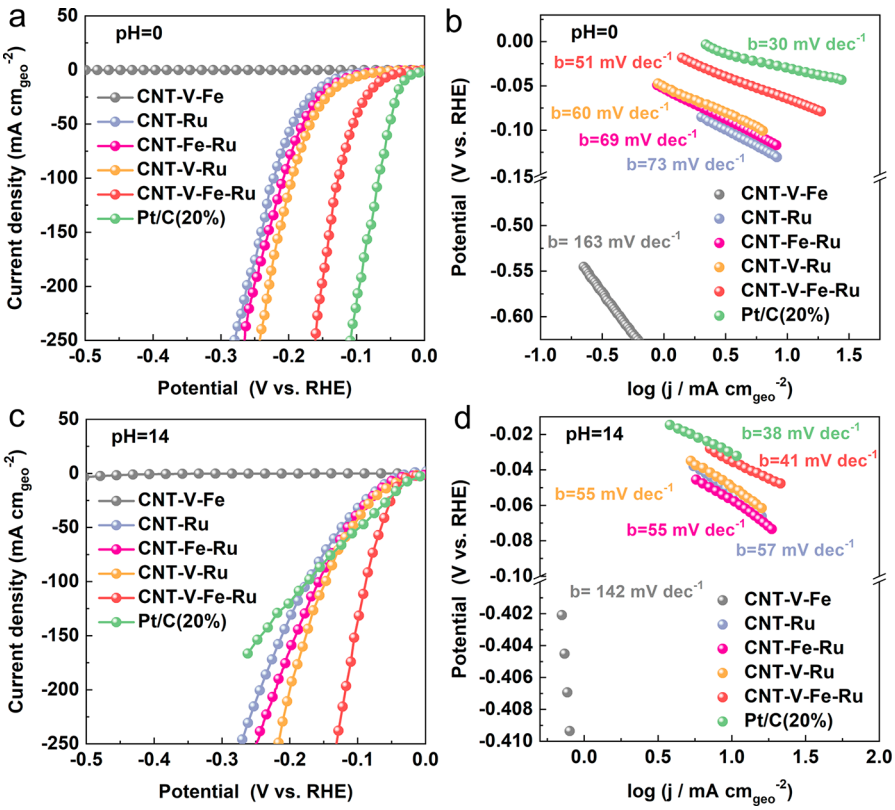

Figure 3. HER electrocatalytic performance (geometric area normalized). (a, c) Polarization curves and (b, d) the corresponding Tafel plots in 0.5 M H_2SO_4 and 1 M KOH, respectively.

(Fe−Fe bond at ca. 2.20 Å) in line with the atomically dispersed Fe sites of the CNT−V−Fe (Figure 2b). Note that the Fe−O bond in CNT−V−Fe at ca. 1.52 Å is different from the Fe−O bond in Fe_2O_3 (the peak at ca. 1.46 Å). Meanwhile, Fe_2O_3 shows an obvious peak at ca. 2.77 Å, assigned to the Fe−Fe interaction in higher shell coordination, while the CNT−V−Fe has not ever shown such signals.[40] These results further strengthen the conclusion of iron sites as isolated single atoms in the as-prepared catalyst instead of Fe_2O_3. Based on the results of FT-EXAFS, the defect-modified Fe−O_4 model structure (Figure S18a) is used to fit the FT-EXAFS spectrum. As shown in Figure S18b−d, the model-based EXAFS fitting results are well fit with the experimental results in *k* and *R* spaces. Based on the fitting results (Table S4), the coordination number is ca. 3.90 and the bonding length is ca. 2.02 Å.

According to the above results, iron single-atom site modified defect-rich CNTs (CNT−V−Fe) are successfully prepared via the iron oxide-induced in situ partial etching functionalization strategy. Then, CNT−V−Fe with unique nanostructure and composition is used as the substrate for anchoring and stabilizing Ru clusters (CNT−V−Fe−Ru). According to the SEM and TEM images of CNT−V−Fe−Ru in Figures S19 and S20 and Figure 2c, small clusters with a diameter of 5−10 nm grow around the defective porous structures, and the lattice fringes of these clusters are determined to be Ru (101). In addition, the characteristic diffraction peaks of metallic ruthenium from XRD patterns (Figure 2g) and the XPS peaks at ca. 280.7 eV ($3d_{5/2}$) and ca. 284.9 ($3d_{3/2}$) in the Ru 3d XPS spectrum (Figure S21) both confirm the successful incorporation of the Ru(0) cluster on CNT−V−Fe.[7,41] Based on the Fe K-edge XANES of CNT−V−Fe−Ru (Figure 2e), the rising-edge position at ca. 7117.1 eV and the obvious pre-edge peaks at ca. 7115.2 eV for CNT−V−Fe−Ru are close to CNT−V−Fe. Therefore, the oxidation state of iron in CNT−V−Fe−Ru is also about +3. The Fourier transform of Fe K-edge EXAFS in Figure 2f shows the decreased absorbance associated with the characteristic signal of the Fe−O bond (the peak at ca. 1.42 Å) after loading Ru clusters compared with that of CNT−V−Fe, implying a decrease of Fe−O coordination number as a result of interaction between iron and ruthenium sites in CNT−V−Fe−Ru. Figure 2h further displays the Ru K-edge XANES of CNT−V−Fe−Ru; the rising-edge position and the obvious pre-edge peak are close to those of the Ru foil, indicating the formation of Ru clusters (0) in CNT−V−Fe−Ru. According to Figure 2i, the peak at ca. 2.41 Å demonstrates that the Ru atom is mainly coordinated with Ru or Fe atoms (Ru−Ru or Ru−Fe).[42] In addition, the decreased absorbance of the Ru−metal bond is likely to be the result of the interfacial interaction between Ru clusters and the substrate. These results reveal the formation of interface structures between Ru clusters and the CNT−V−Fe substrate with the defective iron single-atom (Fe−O_4) moieties via the Ru−Fe bond. Based on the XPS spectra (Figure S21) and XRD patterns (Figure S22) of CNT−Ru, CNT−Fe−Ru, and CNT−V−Ru, metallic Ru is also loaded on CNT, CNT−Fe, and CNT−V. But the particle diameters (>100 nm) of Ru on CNT−Ru, CNT−Fe−Ru, and CNT−V−Ru are much higher than that on CNT−V−Fe−Ru (Figures S23−S25). The abundant vacancy defects in CNT−V−Fe improve the specific surface area (Table S2) and provide more anchor points for the growth of Ru clusters. In addition, the differences in electronegativity for C, O, and Fe as well as the synergistic effects between vacancy defects and oxygen-

https://doi.org/10.1021/acscatal.2c04586
ACS Catal. 2023, 13, 49−59

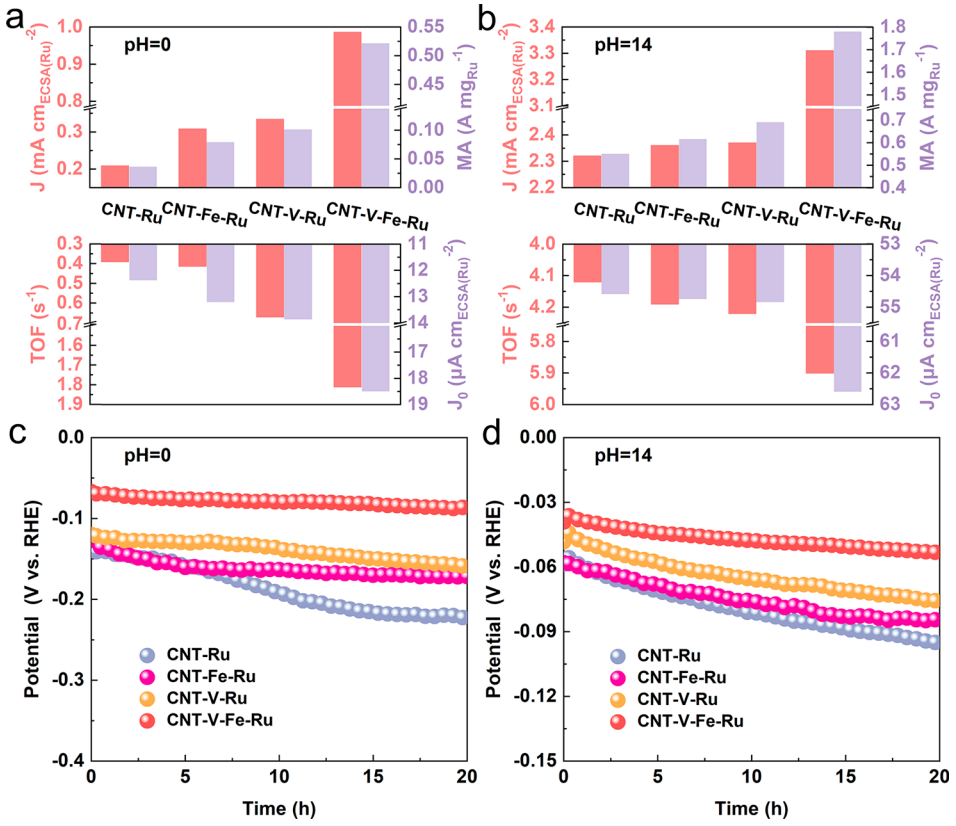

Figure 4. Intrinsic activity analysis of the catalysts. The current density is normalized to ECSA for Ru cluster and Ru mass loading (mass activity (MA)) of the samples at −0.1 V vs RHE; TOF value of the samples at −0.1 V vs RHE and exchange current density (J_0) in (a) 0.5 M H_2SO_4 and (b) 1 M KOH, respectively. (c, d) The stability test of the samples at the current density of 10 mA cm_{geo}^{-2} in 0.5 M H_2SO_4 and 1 M KOH, respectively.

coordinated iron single-atom Fe−O_4 can induce the local charge redistribution to enhance the interfacial interaction between Ru clusters and support.[25,34] These characteristics are beneficial for the firm growth of Ru clusters to avoid the agglomeration of particles during the preparation process. Therefore, CNT−V−Fe−Ru displays high dispersion of Ru clusters.

2.2. Electrocatalytic Performance for the HER. To investigate the effect of the substrates with different interface modifications on HER activity, the electrocatalytic performances of CNT−V−Fe, CNT−Ru, CNT−Fe−Ru, CNT−V−Ru, CNT−V−Fe−Ru, and Pt/C(20%) are first evaluated in 0.5 M H_2SO_4. As shown in Figure 3a, the cathodic polarization current density of CNT−V−Fe is negligible. Via the incorporation of CNT−V−Fe and Ru clusters, CNT−V−Fe−Ru shows a considerable increment of the current density, demonstrating that metallic Ru is an indispensable active site for the HER activity. Among the catalysts with different carbon-based substrates (CNT, CNT−Fe, CNT−V, and CNT−V−Fe), CNT−V−Fe−Ru displays optimal performance with the lowest overpotential of about 64 mV to reach a current density of 10 mA cm_{geo}^{-2}, which is lower than those of CNT−Ru (136 mV), CNT−Fe−Ru (123 mV), and CNT−V−Ru (115 mV) and comparable to most of the reported Ru-based catalytic materials under similar test conditions in Table S5. The Tafel slopes of the catalysts are obtained based on the appropriate overpotential regions, where the catalytic reaction has already taken place and shows a low current density. According to the Tafel plots in Figure 3b, the Tafel slope of CNT−V−Fe−Ru is 51 mV dec^{-1}, indicating that the HER catalyzed by CNT−V−Fe−Ru follows the Volmer−Heyrovský mechanism, and the Heyrovský process is the rate-limiting step, which is different from the hydrogen evolved process on Pt/C(20%) (~30 mV dec^{-1}, Volmer−Tafel mechanism).[43] As shown in Table S6, the Tafel slope of CNT−V−Fe−Ru shows a slight increase as a result of H_2 bubble formation at high overpotentials. Therefore, it is important to obtain the Tafel slope based on appropriate overpotential regions. In addition, the higher Tafel slopes are recorded on CNT−Ru (73 mV dec^{-1}), CNT−Fe−Ru (69 mV dec^{-1}), and CNT−V−Ru (60 mV dec^{-1}) compared with CNT−V−Fe−Ru, suggesting that CNT−V−Fe−Ru can obtain a rapid increase in cathode current density at the same increment of overpotential. To further verify the high catalytic activity of CNT−V−Fe−Ru, the HER activity is further studied in 1.0 M KOH (Figure 3c). As expected, CNT−V−Fe−Ru also exhibits remarkable HER catalytic activity with a low overpotential of 38 mV at 10 mA cm_{geo}^{-2}, which is comparable to Pt/C(20%) (32 mV) and lower than those of CNT−Ru (60 mV), CNT−Fe−Ru (57 mV), and CNT−V−Ru (48 mV), as well as some previously reported Ru-based catalysts (Table S5). According to Figure 3d, the Tafel slope of CNT−V−Fe−Ru is 41 mV dec^{-1}, indicating the same Volmer−Heyrovský mechanism in alkaline electrolytes,[44] which is just slightly higher than that of Pt/C(20%) (38 mV dec^{-1}) but better than CNT−Ru (57 mV dec^{-1}), CNT−Fe−Ru (55 mV dec^{-1}), and CNT−V−Ru (55 mV dec^{-1}). Note that the HER catalytic performance of Pt/C (20%) in alkaline electrolytes is normally worse than that in

https://doi.org/10.1021/acscatal.2c04586
ACS Catal. 2023, 13, 49−59

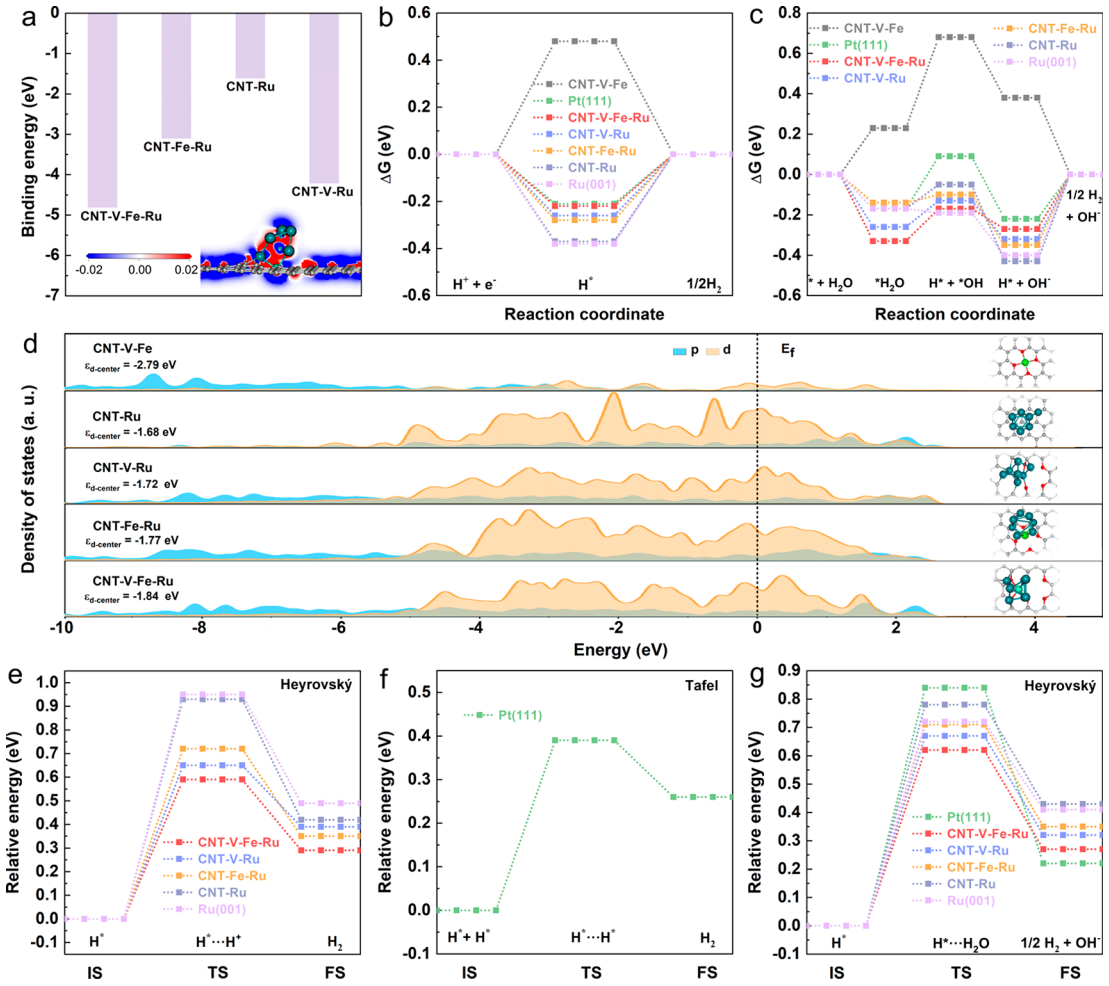

Figure 5. DFT calculations. (a) Binding energy between substrate and Ru clusters for CNT−Ru, CNT−Fe−Ru, and CNT−V−Fe−Ru and the charge density of the CNT−V−Fe−Ru model (the inset). The red and blue clouds represent charge accumulation and depletion with the isosurface energy of 0.02 eV, respectively. (b) Gibbs free energy diagram of H^+ to H_2. (c) Gibbs free energy diagram in alkaline media. (d) PDOS of the potential active site p and d of the H-bonded CNT−V−Fe, CNT−Ru, CNT−Fe−Ru, CNT−V−Ru, and CNT−V−Fe−Ru; the corresponding optimized structures of the active sites (the inset, right). (e, f) Heyrovský activation barriers for Ru-based catalysts and Tafel activation barrier for Pt(111) in acidic media (initial (IS), transition (TS), and final (FS) states). (g) Heyrovský activation barriers of the samples in alkaline media.

acid electrolytes, especially at high current density, due to the more abundant hydrogen ions and faster kinetics in acid media.[45,46] In addition, Pt-based materials show relatively sluggish kinetics in alkaline because of the limitation in the adsorption and dissociation of H_2O.[6,47,48] Nevertheless, Ru sites could facilitate the H_2O adsorption and dissociation process to enhance the HER catalytic performance in alkaline electrolytes.[12,49] Meanwhile, the overstrong Ru−H bonding limits the overall HER reaction particularly in acid, leading to the relatively poor HER performance compared with that in alkaline solutions.[50,51] The electrochemical double-layer capacitance (C_{dl}) is an effective means to estimate the actual electrochemically active surface area (ECSA) of catalysts (ECSA $\propto C_{dl}$).[37,52,53] As depicted in Figure S26, the C_{dl} values follow the order of CNT−V−Fe−Ru (17.41 mF cm^{-2}) > CNT−V−Ru (8.21 mF cm^{-2}) > CNT−Fe−Ru (7.72 mF cm^{-2}) > CNT−Ru (6.70 mF cm^{-2}). The larger C_{dl} for CNT−V−Fe−Ru suggests a higher accessibility of active sites as a result of the porous structures.

CNT−Ru, CNT−Fe−Ru, CNT−V−Ru, and CNT−V−Fe−Ru have obvious differences in composition and micro-structure, thus the LSVs normalized by the geometric area (Figures 3a and c) would not represent the intrinsic activity. To this end, the polarization curves are then normalized by the Ru/Pt mass loading (Table S7) and ECSA of Ru/Pt ($ECSA_{Ru/Pt}$) obtained by the underpotential deposition (UPD) of copper (Figure S27 and Table S8).[54,55] Obviously, CNT−V−Fe−Ru shows the best performance in terms of the mass activity and ECSA-normalized current density (Figures 4, S28, and S29) compared with CNT−Ru, CNT−Fe−Ru, and CNT−V−Ru in both acid and alkaline electrolytes. The exchange current density (J_0) is also obtained from the Tafel plots. As shown in Figure 4, the J_0 values of CNT−V−Fe−Ru (18.5 and 62.6 $\mu A\ cm_{ECSA(Ru)}^{-2}$ in acid and alkaline electrolytes, respectively) are higher than those of CNT−Ru, CNT−Fe−Ru, and CNT−V−Ru, revealing a much faster HER kinetic rate of CNT−V−Fe−Ru.[56] In addition, CNT−V−Fe−Ru also demonstrates the highest turnover frequency (TOF) in comparison with CNT−Ru and CNT−V−Ru (Figures 4, S28, S29), further implying intrinsically more active Ru sites over the CNT−V−Fe substrate. According to the electrochemical impedance spectroscopy (EIS) in Figures S30 and S31, CNT−

https://doi.org/10.1021/acscatal.2c04586
ACS Catal. 2023, 13, 49−59

V−Fe−Ru exhibits the smallest R_{ct} compared with CNT−Ru, CNT−Fe−Ru, and CNT−V−Ru (Figure S32 and Table S9), indicating the fast and efficient charge transfer during the HER catalytic process in both acid and alkaline electrolytes. The catalytic stability test of the catalytic materials is further shown in Figure 4c,d. CNT−V−Fe−Ru displays strong durability, and there is only a slight change in applied potential, which is far better than for CNT−Ru, CNT−Fe−Ru, and CNT−V−Ru with continuously increasing applied potential. The TEM images, XRD patterns, and Ru 3d XPS spectra of CNT−V−Fe−Ru before and after the stability test are shown in Figure S33. The postcatalytic structure composition and dispersion of CNT−V−Fe−Ru did not change evidently, which confirms its high structural and compositional stability. The iron single-atom modified defect-rich porous structures of CNT−V−Fe−Ru provide firm growth sites for Ru clusters and then enhance the interaction in Ru cluster−substrate interfaces, thus obtaining high structure and catalytic stability.

2.3. Theoretical Understanding of the Electronic Structures and HER Mechanism. To further understand the fundamental reason for the efficient HER catalytic performance displayed by CNT−V−Fe−Ru, the density functional theory (DFT) calculations are conducted. The binding energy between Ru clusters and the substrates with different interface modifications (Figure S34) is shown in Figure 5a. The values of binding energy follow the order as CNT−V−Fe−Ru (−4.82 eV) < CNT−V−Ru (−4.22 eV) < CNT−Fe−Ru (−3.11 eV) < CNT−Ru (−1.62 eV). A more negative value of the binding energy for CNT−V−Fe−Ru indicates stronger interaction between Ru clusters and carbon substrates. Namely, Ru sites are likely to be preferentially deposited at the Fe−O_4 moiety with defects to form the atomic and defective interface between Ru clusters and the CNT−V−Fe substrate. In addition, these characteristics can greatly enhance the stability of Ru clusters. Therefore, CNT−V−Fe−Ru displays higher HER catalytic stability than CNT−Ru, CNT−Fe−Ru, and CNT−V−Ru (Figure 4c,d). According to the charge density of the CNT−V−Fe−Ru model (the inset in Figure 5a), the charges of the CNT−V−Fe substrate transfer and accumulate at the Ru cluster, and Ru sites become efficient active centers due to the redistribution of charge between the CNT−V−Fe substrate to Ru clusters, which is favorable for optimizing the adsorption of hydrogen and H_2O (Figures 5b,c).[57] The partial density of states (PDOS) of the potential active sites (Ru or Fe) in CNT−V−Fe, CNT−Ru, CNT−Fe−Ru, CNT−V−Ru, and CNT−V−Fe−Ru after H is absorbed are further compared in Figure 5d. Regarding CNT−V−Fe, Fe-d shows a low electron density near the Fermi level (E_f). But, the Ru-d electron densities near the E_f for the CNT−Ru, CNT−Fe−Ru, CNT−V−Ru, and CNT−V−Fe−Ru are significantly enhanced, which implies Ru sites as the potential active centers for the HER.[15] However, overly strong H adsorption intensity on Ru sites will prohibit the desorption step, thus resulting in a decreased HER performance.[12,13] It is necessary to moderately weaken the H adsorption intensity on Ru sites via introducing substrates to improve catalytic performance.[10] The d centers for CNT−Ru, CNT−Fe−Ru, CNT−V−Ru, and CNT−V−Fe−Ru after H-absorbed are −1.68 eV, −1.77 eV, −1.72 eV, and −1.84 eV, respectively, suggesting that a CNT−V−Fe substrate can decrease the H adsorption intensity of the Ru site to the greatest extent according to the d-band theory.[16,58−60] Thus, CNT−V−Fe−Ru will show efficient HER catalytic performance. To confirm this hypothesis, the free energy differences for H* (ΔG_{H^*}) of CNT−V−Fe, CNT−Ru, CNT−Fe−Ru, CNT−V−Ru, CNT−V−Fe−Ru, Ru (001), and Pt (111) are further compared in Figure 5b. The ΔG_{H^*} of CNT−V−Fe is >0 eV (ΔG_{H^*} = 0.48 eV), suggesting a low H adsorption intensity. The ΔG_{H^*} on Ru (001) is −0.38 eV, suggesting unfavorable HER activity because of the overstrong Ru−H bonding. Nevertheless, the introduction of substrates (CNT, CNT−Fe, CNT−V, and CNT−V−Fe) efficiently wreaks the H adsorption intensity of Ru sites in CNT−Ru (ΔG_{H^*} = −0.37 eV), CNT−Fe−Ru (ΔG_{H^*} = −0.28 eV), CNT−V−Ru (ΔG_{H^*} = −0.26 eV), and CNT−V−Fe−Ru (ΔG_{H^*} = −0.22 eV) compared with Ru (001). The synergistic effect of vacancy defects and iron single-atom sites adequately decreases of H adsorption intensity of Ru sites in CNT−V−Fe−Ru even more, which is consistent with the results of the PDOS. In addition, the ΔG_{H^*} of CNT−V−Fe−Ru is very close to that of Pt (111) (ΔG_{H^*} = −0.21 eV) with state-of-the-art HER activity, following the Sabatier's principle that the optimal hydrogen adsorption free energy (ΔG_{H^*}) of an ideal HER active site is close to zero.[61,62] Therefore, CNT−V−Fe−Ru with the iron single-atomic-site modified defect-rich substrate shows highly efficient HER catalytic performance compared with CNT−V−Fe, CNT−Ru, CNT−Fe−Ru, and CNT−V−Ru, which have been confirmed by the experimental data (Figures 3 and 4). Regarding the water reduction under alkaline conditions, the first step for the HER has been known as the H_2O adsorption and dissociation.[12,49] Specifically, the model of CNT−V−Fe−Ru displays the strongest H_2O adsorption free energy (−0.33 eV, Figure 5c), which greatly benefits the HER process. In addition, the dissociation of the adsorbed water reveals an increase in free energy (potential limiting step), and CNT−V−Fe−Ru shows a lower ΔG = −0.17 eV than those of CNT−Ru, CNT−Fe−Ru, CNT−Fe−Ru, and Pt(111), implying the smallest HER overpotential for the CNT−V−Fe−Ru. In addition, activation energy barriers of the rate-determining step (RDS) on various model catalysts for proton and water reduction (Figures 5e,f and S35) were obtained through the calculation of the searched highest free energy of the transition state (TS). According to the Tafel slopes in Figure 3b, the RDS of CNT−Ru, CNT−Fe−Ru, CNT−V−Ru, and CNT−V−Fe−Ru is the Heyrovský step for the acidic HER, while Pt/C demonstrates the Tafel step as RDS. Thus, the calculated activation barrier of CNT−V−Fe−Ru is 0.59 eV (Figure 5e), which is lower than those of CNT−V−Ru (0.65 eV) and CNT−Fe−Ru (0.72 eV) as well as CNT−Ru (0.93 eV) but higher than that of Pt(111) (0.39 eV, Figure 5f). According to the Tafel slopes for the alkaline water dissociation reaction in Figure 3d, the RDS of all of the Ru-based catalysts and Pt/C is the Heyrovský step. As such, activation barriers on the models are calculated in Figure 5g, where the CNT−V−Fe−Ru displays a much smaller value of 0.62 eV than those of CNT−V−Ru, CNT−Fe−Ru, and CNT−Ru. Moreover, Pt(111) shows the highest energy barrier for the Heyrovský step, which is consistent with our experimental results. Overall, the DFT calculations further strengthen the fundamental understanding of the atomic and defective interface effect on ruthenium clusters under acidic and alkaline conditions.

3. CONCLUSIONS

The unique CNT−V−Fe substrate with abundant vacancy defects and single-atom iron sites (Fe−O_4) is obtained via the iron oxide-induced partial etching for CNTs. Compared with

https://doi.org/10.1021/acscatal.2c04586
ACS Catal. 2023, 13, 49−59

CNT, CNT−Fe, and CNT−V, the iron single-atomic-site modified defect-rich porous structures in CNT−V−Fe promote the high dispersion and firm growth of Ru clusters on the substrate via Ru−Fe bond (CNT−V−Fe−Ru). Therefore, CNT−V−Fe−Ru displays robust HER catalytic performances, including lower overpotential, smaller Tafel slope, bigger J_0 as well as TOF values, and more durable stability in comparison to CNT−Ru, CNT−Fe−Ru, and CNT−V−Ru. The theoretical calculations further prove that the synergistic effect of vacancy defects and iron single-atom sites make CNT−V−Fe−Ru obtain optimal binding energy between Ru clusters and the CNT−V−Fe substrate interface. Meanwhile, the H adsorption intensity of Ru active sites is optimized to the maximum extent possible, thus CNT−V−Fe−Ru displays high HER activity and durable stability. The experimental data and theoretical calculations together reveal the promising application potential of the metal single-atomic-site modified defect-rich substrate for designing efficient catalytic materials. This study, as an important example of single-atom materials serving as advanced supports, is conducive to a deeper insight into the interaction mechanism on metal−substrate interfaces at the atomic level, and more opportunities have light shed on them for broadening the application field of single-atom materials.

4. EXPERIMENTAL SECTION

4.1. The Preparation of the CNT−V−Fe, CNT−V, and CNT−Fe. First, $Fe(NO_3)_3$ (0.2 mmol) was completely dissolved into ethanol solution (30 mL) under stirring. Then, multiwalled carbon nanotubes (CNTs, 200 mg) were added to the above solution under ultrasonic processing. After that, ammonium hydroxide (2 mL, 25 wt %) was introduced to this mixture and then dried in a water bath (60 °C) under stirring to produce uniform powders named CNT−Fe−OH. Next, CNT−Fe−OH was heated to 490 °C at a rate of 10 °C min^{-1} in the air and was kept at this temperature for 60 min. The obtained sample was recorded as CNT−V−Fe−Fe_2O_3. Then, CNT−V−Fe-Fe_2O_3 was dispersed in concentrated hydrochloric acid (10 mL, 36−38 wt %), and the mixture was poured into a Teflon-lined stainless-steel autoclave (25 mL) and heated at 120 °C for 2 h in an oven to remove Fe_2O_3. When the oven cooled to room temperature, the material was washed with deionized water and ethyl alcohol via centrifuge and dried at 60 °C to obtain CNT−V−Fe. In addition, for the sake of contrast, CNT was also treated under the same preparation conditions without the introduction of $Fe(NO_3)_3$ to fabricate CNT−V. The CNT−Fe−OH was heated under the argon flow, and other preparation conditions were the same as CNT−V−Fe to obtain CNT−Fe.

4.2. The Preparation of CNT−V−Fe−Ru, CNT−V−Ru, CNT−Fe−Ru, and CNT−Ru. CNT−V−Fe (2 mg) and $RuCl_3{\cdot}3H_2O$ (0.009 mmol) were dispersed into the solution consisting of distilled water (200 μL), isopropanol (100 μL), and Nafion ionomer (20 μL, 5 wt %) under ultrasonic processing for 30 min. Then, dispersion liquid (4 μL) was dripped to the surface of the glassy carbon electrode. After natural drying, the electrode material was subjected to linear sweep voltammetry scanning from 0.1 to −0.4 V vs the reversible hydrogen electrode (RHE) to fabricate CNT−V−Fe−Ru. CNT−V−Ru, CNT−Fe−Ru, and CNT−Ru, as the controlling samples, were prepared using CNT−V, CNT−Fe, and initial CNT as supporting materials to load Ru compounds via the same preparation processes described above.

4.3. Characterizations. X-ray diffraction (XRD) patterns of the samples were obtained via an X-ray powder diffractometer (CX-2700, Danton, China). The field emission scanning electron microscope (S4800, Hitachi, Japan) was used to observe the surface topography of the samples. High-angle annular dark-field scanning transmission electron microscopy (HAADF-STEM) images were obtained using a probe-corrected transmission electron microscope with aberration correction (JEM-ARM300F, JEOL, Japan). X-ray absorption fine structure spectroscopy (XAFS) analysis, including the X-ray absorption near edge structure (XANES) and extended X-ray absorption fine structure (EXAFS), was performed at the SPring-814b2 beamline of the Synchrotron Radiation Facility of Japan. All samples were characterized using Fe−K edge XANES and EXAFS in transmission mode under ambient conditions with Fe foil as a reference. The IFEFFIT was used to analyze all XAFS data. The chemical valence states of C, O, Fe, and Ru in the samples were analyzed according to the X-ray photoelectron spectra performed on a photoelectron spectroscope (K-Alpha, Thermo Scientific, U.S.A.). The metal contents in the samples were obtained via inductively coupled plasma-optical emission spectroscopy (5110, Agilent, U.S.A.). Nitrogen adsorption−desorption was performed via an automated surface area and pore size analyzer (Quadrasorb Nava 4000, Quantachrome, USA), and specific surface area was obtained by Brunauer−Emmett−Teller (BET) formulations. The thermogravimetric (TG) analysis of the samples was conducted by a simultaneous thermal analyzer (STA4495F5, Netzsch, Germany).

4.4. Electrochemical Measurements. The electrochemical measurements were performed using an electrochemical workstation (204, Autolab, Switzerland) at room temperature. In a three-electrode system, the carbon plate and Ag/AgCl (saturated KCl aqueous solution) electrode were employed as the counter and reference electrodes, while a glassy carbon electrode and carbon paper with loading catalysts served as the working electrode. KOH (1 mol L^{-1}) and H_2SO_4 (0.5 mol L^{-1}) aqueous solutions were used as the electrolytes, respectively. The potentials were transformed to the reversible hydrogen electrode (RHE) based on the calibration equation: $E_{(vsRHE)} = E_{(Ag/AgCl)} + 0.198 + 0.059 \times pH$. Linear sweep voltammetry scanning was performed at a scan rate of 10 mV s^{-1}. The resistances of the electrolyte and charge transfer were obtained by fitting the equivalent circuit (Figure S32 and Table S9) using the Nova software (1.11). Then, the *iR* drops of all electrochemical measurements were then corrected based on the solution resistances. The electrochemical impedance spectra (EIS) of these materials were recorded from 10 kHz to 0.01 Hz.

4.5. Density Functional Theory (DFT) Calculations. The DFT calculations were performed using DMOL[63] code based on Perdew−Burke−Ernzerhof (PBE) functional and the plane-wave pseudopotential for the spin-polarized generalized gradient approximation (GGA).[64,65] The dispersion corrections, including van der Waals interactions, were conducted via the empirical DFT-D method based on the Grimme scheme.[66,67] Metal and oxygen codoped carbon were modeled using a hexagonal 7 × 7 graphene layer containing the metal and oxygen dopants. Ruthenium clusters were modeled with a seven-atom particle. The real-space global orbital cutoff radius of 4.7 Å with a 3 × 3 × 1 k-point grid was used in all calculations. To avoid periodic images' interaction, a vacuum layer (12 Å) perpendicular to the surface was added.

https://doi.org/10.1021/acscatal.2c04586
ACS Catal. 2023, 13, 49−59

The treatment of solvation effects was introduced by using the conductor-like screening model (COSMO).[68,69] The free energy (ΔG) of each elementary step was obtained based on the standard hydrogen electrode model, according to $\Delta G = \Delta E + \Delta E_{ZPE} - T\Delta S$, where ΔS and ΔE are the entropy change and reaction energy, respectively, and ΔE_{ZPE} is the difference between the gas phase and the adsorbed molecules in zero point energy. Activation energy barrier calculations were performed through the search of the transition state of the reaction with the highest free energy. The binding energy is defined as the energy difference between the isolated and the corresponding adsorption systems: $E_{binding} = E_{total} - E_{support} - N \times E_{atom}$, where E_{total}, $E_{support}$, and E_{atom} represent the total energy of the catalyst models with and without Ru clusters and the energy of one Ru atom in the Ru crystal, respectively. N is the number of Ru atoms in Ru clusters ($N = 7$).

■ ASSOCIATED CONTENT

Supporting Information

The Supporting Information is available free of charge at https://pubs.acs.org/doi/10.1021/acscatal.2c04586.

Additional characterization (SEM, TEM, XPS, XRD); N_2 adsorption−desorption isotherms; TG and DTG curves; first-shell fitting parameters of Fe K-edge EXAFS for CNT−V−Fe; double-layer capacitance measurements; and the optimized structures of the catalytic sites (PDF)

■ AUTHOR INFORMATION

Corresponding Authors

Panpan Li − *College of Materials Science and Engineering, Sichuan University, Chengdu 610065, People's Republic of China;* orcid.org/0000-0001-9933-0357; Email: panpanli@scu.edu.cn

Dan Xiao − *Institute for Advanced Study, Chengdu University, Chengdu 610106, People's Republic of China; College of Chemical Engineering, Sichuan University, Chengdu 610065, People's Republic of China;* orcid.org/0000-0001-5295-0540; Email: xiaodan@scu.edu.cn

Zhaoyu Jin − *Institute of Fundamental and Frontier Sciences, University of Electronic Science and Technology of China, Chengdu 610054, People's Republic of China;* orcid.org/0000-0003-0840-3931; Email: zjin@uestc.edu.cn

Authors

Taotao Gao − *Institute for Advanced Study, Chengdu University, Chengdu 610106, People's Republic of China*

Xiangmin Tang − *School of Mechanical Engineering, Chengdu University, Chengdu 610106, People's Republic of China*

Xiaoqin Li − *Institute for Advanced Study, Chengdu University, Chengdu 610106, People's Republic of China*

Shuaiwei Wu − *School of Mechanical Engineering, Chengdu University, Chengdu 610106, People's Republic of China*

Shumin Yu − *School of Mechanical Engineering, Chengdu University, Chengdu 610106, People's Republic of China*

Complete contact information is available at: https://pubs.acs.org/10.1021/acscatal.2c04586

Notes

The authors declare no competing financial interest.

■ ACKNOWLEDGMENTS

P.L. acknowledges the funding support from the National Nature Science Foundation of China (No. 52202372) and Fundamental Research Funds for the Central Universities (YJ2021151). Z.J. acknowledges Fundamental Research Funds for the Central Universities (A1098531023601350). D.X. would like to thank for the support from the National Nature Science Foundation of China (No. 81927809). T.G. acknowledges Chengdu University new faculty start-up funding (No. 2081920074). The authors would like to thank Xie Han from Shiyanjia Lab (www.shiyanjia.com) for the XPS tests.

■ REFERENCES

(1) Turner, J. A. Sustainable Hydrogen Production. *Science* **2004**, *305*, 972−974.

(2) Luo, H.; Barrio, J.; Sunny, N.; Li, A.; Steier, L.; Shah, N.; Stephens, I.; Titirici, M. Progress and Perspectives in Photo- and Electrochemical-Oxidation of Biomass for Sustainable Chemicals and Hydrogen Production. *Adv. Energy Mater.* **2021**, *11*, 2101180.

(3) Tiwari, J.; Sultan, S.; Myung, C.; Yoon, T.; Li, N.; Ha, M.; Harzandi, A.; Park, H.; Kim, D.; Chandrasekaran, S.; Lee, W.; Vij, V.; Kang, H.; Shin, T.; Shin, H.; Lee, G.; Lee, Z.; Kim, K. Multicomponent electrocatalyst with ultralow Pt loading and high hydrogen evolution activity. *Nat. Energy* **2018**, *3*, 773−782.

(4) Yu, X.; Xu, S.; Wang, Z.; Cheng, X.; Du, Y.; Chen, G.; Sun, X.; Wu, Q. An Mn-doped NiCoP flower-like structure as a highly efficient electrocatalyst for hydrogen evolution reaction in acidic and alkaline solutions with long duration. *Nanoscale* **2021**, *13*, 11069−11076.

(5) Li, W.; Liu, Y.; Wu, M.; Feng, X.; Redfern, S.; Shang, Y.; Yong, X.; Feng, T.; Wu, K.; Liu, Z.; Li, B.; Chen, Z.; Tse, J.; Lu, S.; Yang, B. Carbon-Quantum-Dots-Loaded Ruthenium Nanoparticles as an Efficient Electrocatalyst for Hydrogen Production in Alkaline Media. *Adv. Mater.* **2018**, *30*, 1800676.

(6) Mahmood, J.; Li, F.; Jung, S.; Okyay, M.; Ahmad, I.; Kim, S.; Park, N.; Jeong, H.; Baek, J. An efficient and pH-universal ruthenium-based catalyst for the hydrogen evolution reaction. *Nat. Nanotechnol.* **2017**, *12*, 441−446.

(7) Gao, T.; Li, X.; Chen, X.; Zhou, C.; Yue, Q.; Yuan, H.; Xiao, D. Ultra-fast preparing carbon nanotube-supported trimetallic Ni, Ru, Fe heterostructures as robust bifunctional electrocatalysts for overall water splitting. *Chem. Eng. J.* **2021**, *424*, 130416.

(8) Tiwari, J.; Harzandi, A.; Ha, M.; Sultan, S.; Myung, C.; Park, H.; Kim, D.; Thangavel, P.; Singh, A.; Sharma, P.; Chandrasekaran, S.; Salehnia, F.; Jang, J.; Shin, H.; Lee, Z.; Kim, K. High-Performance Hydrogen Evolution by Ru Single Atoms and Nitrided-Ru Nanoparticles Implanted on N-Doped Graphitic Sheet. *Adv. Energy Mater.* **2019**, *9*, 1900931.

(9) Tiwari, J.; Dang, N.; Sultan, S.; Thangavel, P.; Jeong, H.; Kim, K. Multi-heteroatom-doped carbon from waste-yeast biomass for sustained water splitting. *Nat. Sustain.* **2020**, *3*, 556−563.

(10) Ding, R.; Lin, L.; Pei, C.; Yu, X.; Sun, Q.; Park, H. Hierarchical Architectures Based on Ru Nanoparticles/Oxygen-Rich-Carbon Nanotubes for Efficient Hydrogen Evolution. *Chem.—Eur. J.* **2021**, *27*, 11150−11157.

(11) Wang, Q.; Ming, M.; Niu, S.; Zhang, Y.; Fan, G.; Hu, J. Scalable Solid-State Synthesis of Highly Dispersed Uncapped Metal (Rh, Ru, Ir) Nanoparticles for Efficient Hydrogen Evolution. *Adv. Energy Mater.* **2018**, *8*, 1801698.

(12) Zheng, Y.; Jiao, Y.; Zhu, Y.; Li, L. H.; Han, Y.; Chen, Y.; Jaroniec, M.; Qiao, S. High Electrocatalytic Hydrogen Evolution Activity of an Anomalous Ruthenium Catalyst. *J. Am. Chem. Soc.* **2016**, *138*, 16174−16181.

(13) Zheng, J.; Sheng, W.; Zhuang, Z.; Xu, B.; Yan, Y. Universal dependence of hydrogen oxidation and evolution reaction activity of platinum-group metals on pH and hydrogen binding energy. *Sci. Adv.* **2016**, *2*, e1501602.

(14) Wu, X.; Wang, Z.; Zhang, D.; Qin, Y.; Wang, M.; Han, Y.; Zhan, T.; Yang, B.; Li, S.; Lai, J.; Wang, L. Solvent-free microwave synthesis of ultra-small Ru-Mo_2C@CNT with strong metal-support interaction for industrial hydrogen evolution. *Nat. Commun.* **2021**, *12*, 4018.
(15) Zhang, D.; Wang, Z.; Wu, X.; Shi, Y.; Nie, N.; Zhao, H.; Miao, H.; Chen, X.; Li, S.; Lai, J.; Wang, L. Noble Metal (Pt, Rh, Pd, Ir) Doped Ru/CNT Ultra-Small Alloy for Acidic Hydrogen Evolution at High Current Density. *Small* **2022**, *18*, 2104559.
(16) Shi, Y.; Ma, Z. R.; Xiao, Y.; Yin, Y.; Huang, W.; Huang, Z.; Zheng, Y.; Mu, F.; Huang, R.; Shi, G.; Sun, Y.; Xia, X.; Chen, W. Electronic metal-support interaction modulates single-atom platinum catalysis for hydrogen evolution reaction. *Nat. Commun.* **2021**, *12*, 3021.
(17) Qiu, W.; Chen, X.; Liu, Y.; Xiao, D.; Wang, P.; Li, R.; Liu, K.; Jin, Z.; Li, P. Confining intermediates within a catalytic nanoreactor facilitates nitrate-to-ammonia electrosynthesis. *Appl. Catal. B: Environ.* **2022**, *315*, 121548.
(18) Luo, Y.; Li, P.; Jin, Z. Lithiated interface of Pt/TiO_2 enables an efficient wire-shaped Zn-Air solar micro-battery. *Chem. Commun.* **2022**, *58*, 5988−5991.
(19) Jin, Z.; Bard, A. Surface Interrogation of Electrodeposited MnO_x and $CaMnO_3$ Perovskites by Scanning Electrochemical Microscopy: Probing Active Sites and Kinetics for the Oxygen Evolution Reaction. *Angew. Chem., Int. Ed.* **2021**, *60*, 794−799.
(20) Wang, H.; Shao, Y.; Mei, S.; Lu, Y.; Zhang, M.; Sun, J.; Matyjaszewski, K.; Antonietti, M.; Yuan, J. Polymer-Derived Heteroatom-Doped Porous Carbon Materials. *Chem. Rev.* **2020**, *120*, 9363−9419.
(21) Wu, G.; Dai, C.; Wang, D.; Li, D.; Li, N. Nitrogen-doped magnetic onion-like carbon as support for Pt particles in a hybrid cathode catalyst for fuel cells. *J. Mater. Chem.* **2010**, *20*, 3059−3068.
(22) Liang, Q.; Li, Q.; Xie, L.; Zeng, H.; Zhou, S.; Huang, Y.; Yan, M.; Zhang, X.; Liu, T.; Zeng, J.; Liang, K.; Terasaki, O.; Zhao, D.; Jiang, L.; Kong, B. Superassembly of Surface-Enriched Ru Nanoclusters from Trapping-Bonding Strategy for Efficient Hydrogen Evolution. *ACS Nano* **2022**, *16*, 7993−8004.
(23) Fu, X.; Zhang, P.; Sun, T.; Xu, L.; Gong, L.; Chen, B.; Xu, Q.; Zheng, T.; Yu, Z.; Chen, X.; Zhang, S.; Hou, M.; Wang, H.; Wang, K.; Jiang, J. Atomically Dispersed Ni-N_3 Sites on Highly Defective Micro-Mesoporous Carbon for Superior CO_2 Electroreduction. *Small* **2022**, *18*, 2107997.
(24) Song, Q.; Qiao, X.; Liu, L.; Xue, Z.; Huang, C.; Wang, T. Ruthenium@N-doped graphite carbon derived from carbon foam for efficient hydrogen evolution reaction. *Chem. Commun.* **2019**, *55*, 965−968.
(25) Qiao, Z.; Wang, C.; Li, C.; Zeng, Y.; Hwang, S.; Li, B.; Karakalos, S.; Park, J.; Kropf, A.; Wegener, E.; Gong, Q.; Xu, H.; Wang, G.; Myers, D.; Xie, J.; Spendelow, J.; Wu, G. Atomically dispersed single iron sites for promoting Pt and Pt_3Co fuel cell catalysts: performance and durability improvements. *Energy Environ. Sci.* **2021**, *14*, 4948−4960.
(26) Li, P.; Jin, Z.; Fang, Z.; Yu, G. A single-site iron catalyst with preoccupied active centers that achieves selective ammonia electrosynthesis from nitrate. *Energy Environ. Sci.* **2021**, *14*, 3522−3531.
(27) Jin, Z.; Li, P.; Fang, Z.; Yu, G. Emerging Electrochemical Techniques for Probing Site Behavior in Single-Atom Electrocatalysts. *Acc. Chem. Res.* **2022**, *55*, 759−769.
(28) Jin, Z.; Li, P.; Meng, Y.; Fang, Z.; Xiao, D.; Yu, G. Understanding the inter-site distance effect in single-atom catalysts for oxygen electroreduction. *Nat. Catal.* **2021**, *4*, 615−622.
(29) Li, P.; Jin, Z.; Qian, Y.; Fang, Z.; Xiao, D.; Yu, G. Supramolecular confinement of single Cu atoms in hydrogel frameworks for oxygen reduction electrocatalysis with high atom utilization. *Mater. Today* **2020**, *35*, 78−86.
(30) Li, P.; Fang, Z.; Jin, Z.; Yu, G. Ammonia electrosynthesis on single-atom catalysts: Mechanistic understanding and recent progress. *Chem. Phys. Rev.* **2021**, *2*, 041305.
(31) Wang, P.; Jin, Z.; Li, P.; Yu, G. Design principles of hydrogen-evolution-suppressing single-atom catalysts for aqueous electrosynthesis. *Chem. Catal.* **2022**, *2*, 1277−1287.
(32) Jin, Z.; Bard, A. Atom-by-atom electrodeposition of single isolated cobalt oxide molecules and clusters for studying the oxygen evolution reaction. *Proc. Natl. Acad. Sci. U. S. A.* **2020**, *117*, 12651.
(33) Ao, X.; Zhang, W.; Zhao, B.; Ding, Y.; Nam, G.; Soule, L.; Abdelhafiz, A.; Wang, C.; Liu, M. Atomically dispersed Fe-N-C decorated with Pt-alloy core-shell nanoparticles for improved activity and durability towards oxygen reduction. *Energy Environ. Sci.* **2020**, *13*, 3032−3040.
(34) Liang, L.; Jin, H.; Zhou, H.; Liu, B.; Hu, C.; Chen, D.; Wang, Z.; Hu, Z.; Zhao, Y.; Li, H.; He, D.; Mu, S. Cobalt single atom site isolated Pt nanoparticles for efficient ORR and HER in acid media. *Nano Energy* **2021**, *88*, 106221.
(35) Pimenta, M.; Dresselhaus, G.; Dresselhaus, M.; Cançado, L.; Jorio, A.; Saito, R. Studying disorder in graphite-based systems by Raman spectroscopy. *Phys. Chem. Chem. Phys.* **2007**, *9*, 1276−1290.
(36) Pan, D.; Wang, S.; Zhao, B.; Wu, M.; Zhang, H.; Wang, Y.; Jiao, Z. Li Storage Properties of Disordered Graphene Nanosheets. *Chem. Mater.* **2009**, *21*, 3136−3142.
(37) Gao, T.; Zhou, C.; Zhang, Y.; Jin, Z.; Yuan, H.; Xiao, D. Ultra-fast pyrolysis of ferrocene to form Fe/C heterostructures as robust oxygen evolution electrocatalysts. *J. Mater. Chem. A* **2018**, *6*, 21577−21584.
(38) Zhang, S.; Jin, M.; Shi, T.; Han, M.; Sun, Q.; Lin, Y.; Ding, Z.; Zheng, L. R.; Wang, G.; Zhang, Y.; Zhang, H.; Zhao, H. Electrocatalytically Active Fe-$(O\text{-}C_2)_4$ Single-Atom Sites for Efficient Reduction of Nitrogen to Ammonia. *Angew. Chem., Int. Ed.* **2020**, *59*, 13423−13429.
(39) Li, X.; Guo, Y.; Gao, T.; Li, P.; Jin, Z.; Xiao, D. Interconnecting 3D Conductive Networks with Nanostructured Iron/Iron Oxide Enables a High-Performance Flexible Battery. *ACS Appl. Mater. Interfaces* **2021**, *13*, 57411−57421.
(40) Yin, Y.; Shi, L.; Li, W.; Li, X.; Wu, H.; Ao, Z.; Tian, W.; Liu, S.; Wang, S.; Sun, H. Boosting Fenton-Like Reactions via Single Atom Fe Catalysis. *Environ. Sci. Technol.* **2019**, *53*, 11391−11400.
(41) Liu, X.; Jiang, G.; Tan, Y.; Luo, S.; Xu, M.; Jia, Y.; Lu, P.; He, Y. Highly-dispersed ruthenium precursors via a self-assembly-assisted synthesis of uniform ruthenium nanoparticles for superior hydrogen evolution reaction. *RSC Adv.* **2020**, *10*, 14313−14316.
(42) Hu, C.; Song, E.; Wang, M.; Chen, W.; Huang, F.; Feng, Z.; Liu, J.; Wang, J. Partial-Single-Atom, Partial-Nanoparticle Composites Enhance Water Dissociation for Hydrogen Evolution. *Adv. Sci.* **2021**, *8*, 2001881.
(43) Kong, X.; Xu, K.; Zhang, C.; Dai, J.; Norooz Oliaee, S.; Li, L.; Zeng, X.; Wu, C.; Peng, Z. Free-Standing Two-Dimensional Ru Nanosheets with High Activity toward Water Splitting. *ACS Catal.* **2016**, *6*, 1487−1492.
(44) Liang, K.; Pakhira, S.; Yang, Z.; Nijamudheen, A.; Ju, L.; Wang, M.; Aguirre-Velez, C.; Sterbinsky, G.; Du, Y.; Feng, Z.; Mendoza-Cortes, J.; Yang, Y. S-Doped MoP Nanoporous Layer Toward High-Efficiency Hydrogen Evolution in pH-Universal Electrolyte. *ACS Catal.* **2019**, *9*, 651−659.
(45) Subbaraman, R.; Tripkovic, D.; Strmcnik, D.; Chang, K.-C.; Uchimura, M.; Paulikas, A. P.; Stamenkovic, V.; Markovic, N. M. Enhancing Hydrogen Evolution Activity in Water Splitting by Tailoring Li^+-Ni$(OH)_2$-Pt Interfaces. *Science* **2011**, *334*, 1256−1260.
(46) Danilovic, N.; Subbaraman, R.; Strmcnik, D.; Chang, K.; Paulikas, P.; Stamenkovic, R.; Markovic, M. Enhancing the Alkaline Hydrogen Evolution Reaction Activity through the Bifunctionality of Ni$(OH)_2$/Metal Catalysts. *Angew. Chem., Int. Ed.* **2012**, *51*, 12495−12498.
(47) Cheng, Q.; Hu, C.; Wang, G.; Zou, Z.; Yang, H.; Dai, L. Carbon-Defect-Driven Electroless Deposition of Pt Atomic Clusters for Highly Efficient Hydrogen Evolution. *J. Am. Chem. Soc.* **2020**, *142*, 5594−5601.

https://doi.org/10.1021/acscatal.2c04586
ACS Catal. 2023, 13, 49−59

(48) Yu, F.; Lang, Z.; Yin, L.; Feng, K.; Xia, Y.; Tan, H.; Zhu, H.; Zhong, J.; Kang, Z.; Li, Y. Pt-O bond as an active site superior to Pt0 in hydrogen evolution reaction. *Nat. Commun.* **2020**, *11*, 490.
(49) Zheng, Y.; Jiao, Y.; Vasileff, A.; Qiao, S. The Hydrogen Evolution Reaction in Alkaline Solution: From Theory, Single Crystal Models, to Practical Electrocatalysts. *Angew. Chem., Int. Ed.* **2018**, *57*, 7568−7579.
(50) Li, Y.; He, J.; Cheng, W.; Su, H.; Li, C.; Zhang, H.; Liu, M.; Zhou, W.; Chen, X.; Liu, Q. High mass-specific reactivity of a defect-enriched Ru electrocatalyst for hydrogen evolution in harsh alkaline and acidic media. *Sci. China Mater.* **2021**, *64*, 2467−2476.
(51) Jiao, Y.; Zheng, Y.; Jaroniec, M.; Qiao, S. Design of electrocatalysts for oxygen- and hydrogen-involving energy conversion reactions. *Chem. Soc. Rev.* **2015**, *44*, 2060−2086.
(52) Gao, T.; Jin, Z.; Liao, M.; Xiao, J.; Yuan, H.; Xiao, D. A trimetallic V-Co-Fe oxide nanoparticle as an efficient and stable electrocatalyst for oxygen evolution reaction. *J. Mater. Chem. A* **2015**, *3*, 17763−17770.
(53) Yoon, Y.; Yan, B.; Surendranath, Y. Suppressing Ion Transfer Enables Versatile Measurements of Electrochemical Surface Area for Intrinsic Activity Comparisons. *J. Am. Chem. Soc.* **2018**, *140*, 2397−2400.
(54) Green, C.; Kucernak, A. Determination of the Platinum and Ruthenium Surface Areas in Platinum-Ruthenium Alloy Electrocatalysts by Underpotential Deposition of Copper. I. Unsupported Catalysts. *J. Phys. Chem. B* **2002**, *106*, 1036−1047.
(55) Łosiewicz, B.; Martin, M.; Lebouin, C.; Lasia, A. Kinetics of hydrogen underpotential deposition at ruthenium in acidic solutions. *J. Electroanal. Chem.* **2010**, *649*, 198−205.
(56) Men, Y.; Li, P.; Zhou, J.; Cheng, G.; Chen, S.; Luo, W. Tailoring the Electronic Structure of Co_2P by N Doping for Boosting Hydrogen Evolution Reaction at All pH Values. *ACS Catal.* **2019**, *9*, 3744−3752.
(57) Zhao, Y.; Wang, X.; Cheng, G.; Luo, W. Phosphorus-Induced Activation of Ruthenium for Boosting Hydrogen Oxidation and Evolution Electrocatalysis. *ACS Catal.* **2020**, *10*, 11751−11757.
(58) Jiang, Y.; Yu, F.; Que, L.; Deng, L.; Xia, Y.; Ke, W.; Han, Y.; Wang, Z. Revealing the Thermodynamics and Kinetics of In-Plane Disordered Li_2MnO_3 Structure in Li-Rich Cathodes. *ACS Energy Lett.* **2021**, *6*, 3836−3843.
(59) Yu, J.; Li, J.; Xu, C. Y.; Li, Q.; Liu, Q.; Liu, J.; Chen, R.; Zhu, J.; Wang, J. Modulating the d-band centers by coordination environment regulation of single-atom Ni on porous carbon fibers for overall water splitting. *Nano Energy* **2022**, *98*, 107266.
(60) Nørskov, J. K.; Abild-Pedersen, F.; Studt, F.; Bligaard, T. Density functional theory in surface chemistry and catalysis. *Proc. Natl. Acad. Sci. U. S. A.* **2011**, *108*, 937−943.
(61) Nørskov, J.; Bligaard, T.; Logadottir, A.; Kitchin, J.; Chen, J.; Pandelov, S.; Stimming, U. Trends in the Exchange Current for Hydrogen Evolution. *J. Electrochem. Soc.* **2005**, *152*, J23.
(62) Sheng, W.; Myint, M.; Chen, J.; Yan, Y. Correlating the hydrogen evolution reaction activity in alkaline electrolytes with the hydrogen binding energy on monometallic surfaces. *Energy Environ. Sci.* **2013**, *6*, 1509−1512.
(63) Kwak, J.; Bard, A. Scanning electrochemical microscopy. Theory of the feedback mode. *Anal. Chem.* **1989**, *61*, 1221−1227.
(64) Delley, B. An all-electron numerical method for solving the local density functional for polyatomic molecules. *J. Chem. Phys.* **1990**, *92*, 508−517.
(65) Delley, B. From molecules to solids with the $DMol^3$ approach. *J. Chem. Phys.* **2000**, *113*, 7756−7764.
(66) Grimme, S.; Antony, J.; Ehrlich, S.; Krieg, H. A consistent and accurate ab initio parametrization of density functional dispersion correction (DFT-D) for the 94 elements H-Pu. *J. Chem. Phys.* **2010**, *132*, 154104.
(67) Grimme, S. Accurate description of van der Waals complexes by density functional theory including empirical corrections. *J. Comput. Chem.* **2004**, *25*, 1463−1473.
(68) Delley, B. The conductor-like screening model for polymers and surfaces. *Mol. Simul.* **2006**, *32*, 117−123.
(69) Klamt, A.; Schuurmann, G. COSMO: a new approach to dielectric screening in solvents with explicit expressions for the screening energy and its gradient. *J. Chem. Soc., Perkin Trans.* **1993**, *2*, 799−805.

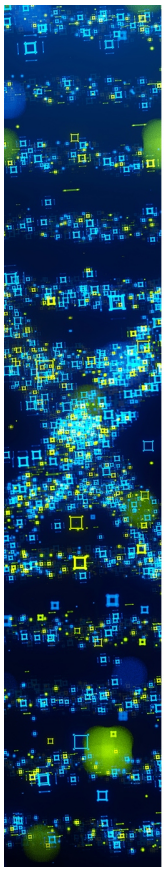
CAS BIOFINDER DISCOVERY PLATFORM™
STOP DIGGING THROUGH DATA —START MAKING DISCOVERIES
CAS BioFinder helps you find the right biological insights in seconds
Start your search
CAS
A division of the American Chemical Society

https://doi.org/10.1021/acscatal.2c04586
ACS Catal. 2023, 13, 49−59